



CHORUS

This is the accepted manuscript made available via CHORUS. The article has been published as:

Polar structure of disclination loops in nematic liquid crystals probed by second-harmonic-light scattering

Shokir A. Pardaev, J. C. Williams, R. J. Twieg, A. Jakli, J. T. Gleeson, B. Ellman, and S. Sprunt

Phys. Rev. E **91**, 032501 — Published 11 March 2015

DOI: [10.1103/PhysRevE.91.032501](https://doi.org/10.1103/PhysRevE.91.032501)

Polar structure of disclination loops in nematic liquid crystals probed by second harmonic light scattering

Shokir A. Pardaev^a, J. C. Williams^b, R. J. Twieg^b, A. Jakli^c, J. T. Gleeson^a, B. Ellman,^a and S. Sprunt^a

^a *Department of Physics, Kent State University, Kent, Ohio 44242*

^b *Department of Chemistry and Biochemistry, Kent State University, Kent, Ohio 44242 USA and*

^c *Chemical Physics Interdisciplinary Program and Liquid Crystal Institute, Kent State University, Kent, OH 44242 USA*

(Dated: February 17, 2015)

Angle-resolved, second harmonic light scattering (SHLS) measurements are reported for three different classes of thermotropic nematic liquid crystals (NLCs): polar and nonpolar rodlike compounds and a bent-core compound. Results revealing well-defined scattering peaks are interpreted in terms of the electric polarization induced by distortions of the nematic orientational field (“flexopolarity”) associated with inversion wall defects – non-singular disclinations, analogous to Neel walls in ferromagnets, that often exhibit a closed loop morphology in NLCs. Analysis of the SHLS patterns based on this model provides a “proof-of-concept” for a new approach to probe the flexopolar properties of NLCs.

PACS numbers: 71.10.Hf, 71.27.+a, 74.70.Tx

I. INTRODUCTION

Although their molecular constituents can be strongly polar (with individual dipole moments ranging up to ~ 10 Debye), ordinary nematic liquid crystals (NLCs) are centrosymmetric materials. When averaged over a few molecular lengths, the electric polarization vanishes, and the orientational order is characterized purely by a second-rank tensor order parameter representing, e.g., the anisotropic part of the linear dielectric response. However, centrosymmetry may be broken in NLCs due either to a distortion of the nematic ordering axis (director \mathbf{n}), producing an electric polarization via the so-called “flexoelectric” effect [1], or to a spatial variation in the magnitude of the nematic order parameter itself (“order” electricity). Microscopically, the polarization depends both on single molecule properties (shape, flexibility, charge distribution) and on the extent and nature of intermolecular correlations. While the polarization induced by director distortions (“flexopolarity”) is typically quite small in rod-like nematics, the recent development of new classes of reduced symmetry nematic mesogens [2], and the discovery of novel nematic phases (e.g., the twist-bend phase [3]), have rekindled interest in non-centrosymmetric/polar structure in NLCs and in techniques that may be used to probe it.

Second harmonic generation (SHG) is arguably the most powerful such technique. SHG has been extensively used to investigate both the orientational anchoring of nematics at boundary surfaces (where non-centrosymmetry is permitted) [4] and to probe variations in the orientational field in thin layers near the surfaces of nematic films [5] under conditions where surface and bulk orientations compete. Fewer studies have focused on noncentrosymmetry and second harmonic generation associated primarily with bulk phenomena in NLCs. Thermal fluctuations of \mathbf{n} are one source of (transient) non-centrosymmetry in the bulk; these not only cause copious linear light scattering, but also generate SH light

due to the flexoelectric polarization induced by orientational fluctuations. However, though investigated in some detail in earlier studies [6, 7], the SH signal associated with director fluctuations is typically quite weak and shows much weaker angular dependence compared to linear scattering.

This paper reports on second harmonic light scattering (SHLS) from a quasistatic source: topological defects in \mathbf{n} , which also locally break centrosymmetry. Our main purpose is to demonstrate a new approach for probing the polar structure of these defects, which spontaneously form in NLCs. We describe a model that relates our experimental results to the properties of a specific type of nematic disclination, known as an *inversion wall loop* [8], across which \mathbf{n} varies analogously to the magnetization across Neel walls in ferromagnets. The model is motivated by direct imagery of these loops, stabilized at the surfaces of three different types of thermotropic NLC we have investigated, and is also inspired by an interesting connection to theoretical and experimental SHLS studies in other complex fluids – namely, colloidal suspensions containing centrosymmetric particles covered with a monolayer of non-centrosymmetric dye [9–12]. As a secondary outcome, our results and analysis provide a “proof-of-concept” of a potentially new technique to characterize the flexoelectric properties of NLCs, based on combining SHLS with known profiles of \mathbf{n} associated with nematic disclinations. In the concluding section, we suggest pathways for future development of this technique, which could ultimately provide novel quantitative information about the individual material coefficients associated with flexoelectricity. This is especially relevant in light of a recent upsurge of interest in flexoelectric studies of both nonchiral and chiral fluid phases of liquid crystals [13–16] and due to the fact that conventional methods typically probe only linear combinations of the coefficients (often giving conflicting results [14]).

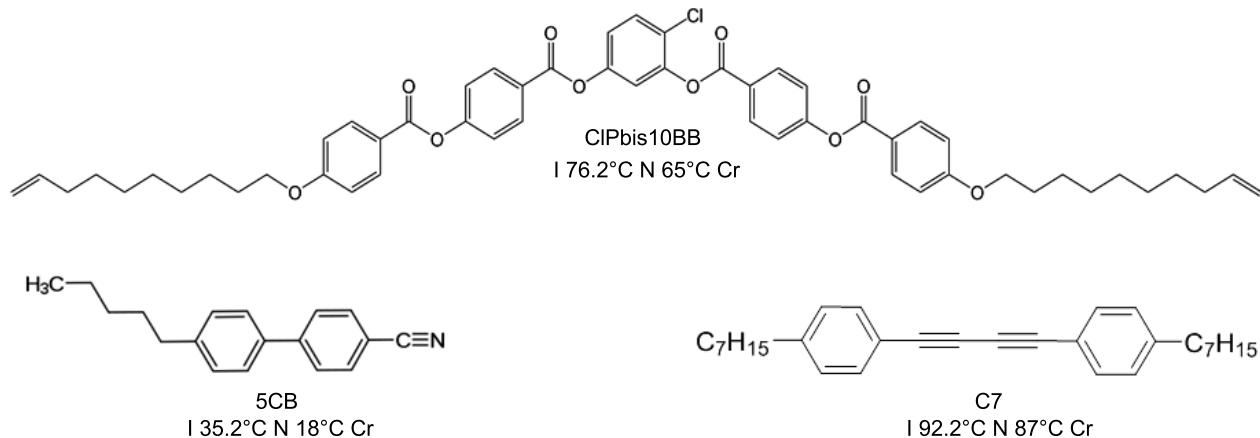


FIG. 1. Chemical structures and transition temperatures for the liquid crystal molecules studied.

II. EXPERIMENTAL DETAILS

The chemical structures and nematic ranges of the three NLC materials studied are presented in Fig. 1. They comprise examples from three classes of thermotropic compounds: polar and nonpolar rodlike mesogens – 4-Cyano-4'-pentylbiphenyl or 5CB and 1-heptyl-4-[4-(4-heptylphenyl)buta-1,3-diyne-1-yl]benzene or C7 [17], respectively – as well as a bow shaped (bent-core) nematic compound – 4-chloro-1,3-phenylenebis-4-[4-(9-decenyloxy)benzoyloxy]benzoate [18], which we simply designate BCN. This BCN and closely related compounds exhibit unusual properties – including short-range smectic-C-like molecular correlations [19], non-Newtonian flow behavior [20], unusual viscoelastic anisotropy [21], and large electromechanical coupling [22] – even though their macroscopic orientational order is of the conventional (uniaxial) type.

The nematic samples were loaded into custom-made fused silica optical cuvettes with bare (untreated) interior surfaces and with inside width and path length of 6.5 and 1 mm, respectively. The cuvettes were placed in a temperature controlled oven with optical access through thin fused silica windows. The surfaces of the cuvettes were not treated for any particular molecular anchoring. The oven was situated between the pole faces of an electromagnet, which produces a 1.13 T field to align the nematic director (average long molecular axis in all cases) along a horizontal direction in the lab parallel to the cuvette surfaces [23]. Prior to measurements, the samples were heated to the isotropic phase, cooled at $\sim 1^\circ\text{C}/\text{min}$ in the field, and then examined optically in order to confirm a homogeneous nematic state.

The major components of our experimental setup for SHLS are summarized in Fig. 2. A Nd:YAG laser (Continuum Minilite II) operating at 1064 nm delivered 5-7 ns,

typically 2 mJ optical pulses at 10 Hz to the nematic samples, which are located ~ 1 m from the laser head, where the beam has a nearly Gaussian profile. The beam was normally incident on the sample cell and also normal to the direction of the applied magnetic field (and thus to the average \mathbf{n}). The incident polarization could be rotated by a half-wave plate between a vertical (V) orientation, which is perpendicular to both the incident wavevector and to the field direction, and a horizontal (H) direction parallel to the field. Just before the sample, the laser beam was passed through a 1064 nm (10 nm FWHM) laser line filter, in order to remove any coaxial radiation (e.g., light from the flashlamp) containing the second harmonic at 532 nm, and was apertured down to a 1 mm waist.

The second harmonic light emitted from the sample was collected over a cone around the forward direction by a home-made optical telescope. The telescope, which combines a 50 mm diameter precision aspheric lens (0.83 N.A.) and two 50.8 mm diameter achromats (Edmund Optics TECHSPEC series), reconstructs the pattern of SH radiation emitted from the sample on the surface of a 512×512 pixel, cooled CCD detector inside a low noise camera (Princeton Instruments, ProEM512). The lens combination maps parallel rays emerging from the sample at angle θ (measured from the incident IR direction) onto convergent (focused) rays in a plane where the angular acceptance of the CCD from the imaged source (i.e., from the image of the illuminated sample volume) is approximately $\pm 15^\circ$. This proved an ideal match for the scattering patterns from our samples. Additionally, the focusing effect proved useful for defining the angular position of the peak SH scattering, but sacrificed information on the true peak width. In the portion of the telescope where the rays are nearly collimated are two Schott glass IR-cut filters and a 532 nm (1 nm FWHM) laser line filter that eliminate the 1064 nm fundamental and narrowly pass the second harmonic, while also re-

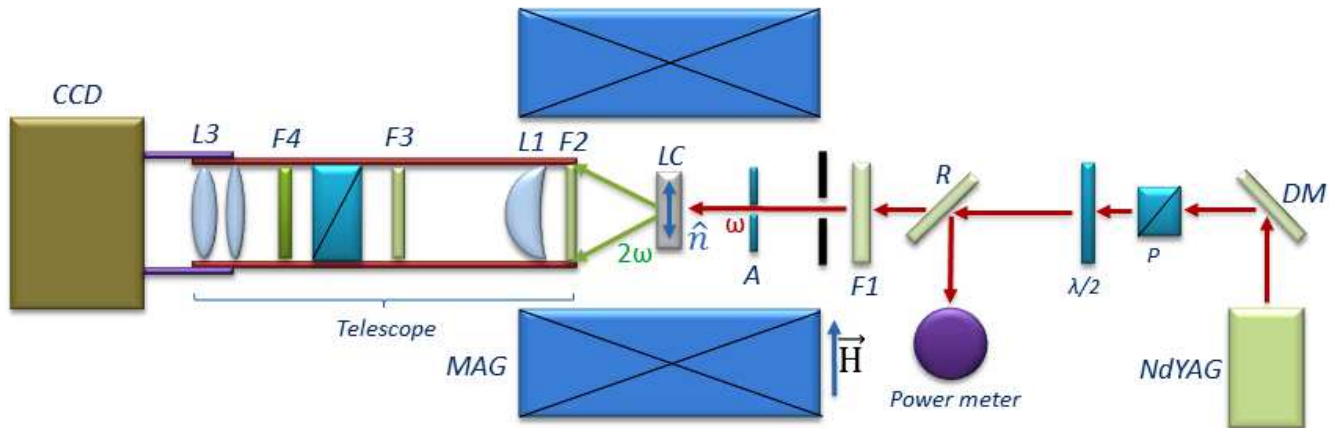


FIG. 2. Schematic diagram of the experimental setup.

ducing the contribution of any multi-photon fluorescence to background level. The telescope also contains an analyzer that can be rotated to select V or H polarization of the second harmonic light.

In the presentation and discussion of our results in subsequent sections, we will only be interested in the angular peak position and will not be concerned with the peak width. The angle θ was calibrated against pixel position on the CCD both by ray tracing software (using the specified lens parameters) and also by direct measurement of the diffraction pattern from a solution of polystyrene spheres of known diameter placed at the sample position and illuminated with 543 nm laser light. The latter calibration was performed after adjusting the camera position to center the scattering pattern on the CCD and to subtend a suitable angular range.

The angular distribution of the SH radiation was recorded at various temperatures in the nematic phase. Typical exposure times were 300–600 s. All measurements were made in a darkened room, with care taken to eliminate stray sources of light from instrumentation. The complete setup, minus any liquid crystal, produced no detectable signal above the camera noise level. The incident IR pulse energy was also monitored, and the detected SH power was normalized to the square of this energy. (Typical variations in the pulse energy setting were $< 10\%$.)

Over several weeks, we observed no evidence of laser damage to the samples at the pulse energies used. Other than a weak halo due to scattering from director fluctuations, no unusual distortion was observed in the shape of the IR beam transmitted through the sample. Moreover, the peak intensity of the incident beam employed in the present experiment was an order of magnitude lower than that used in previous SHLS studies on 5CB, which caused no light-induced distortions or heating within the sample [6].

III. RESULTS

Fig. 3 presents representative results for the angular patterns of SHLS recorded from the three magnetically-aligned nematics studied at a temperature 2.2°C below the nematic-isotropic transition (T_{NI}). These data correspond to a VV polarizer/analyzer setting and thus to a $V(\omega) \rightarrow V(2\omega)$ scattering process. The top row of Fig. 3 shows raw images from the camera, while the bottom row displays the corresponding SH power, as a function of scattering angle θ , integrated over a vertical band of the ± 15 pixels around the horizontal axis through the center of the images. (Here $\theta = 0$ corresponds to the direction of the incident IR beam and to the central point in the images.) To establish that the recorded power ($P_{2\omega}$) does indeed originate from second harmonic generation, we measured $P_{2\omega}$ for a range of IR pulse energies (E_ω) at $T_{NI} - T = 2.2^\circ\text{C}$. The results in Fig. 4 confirm the expected relation $P_{2\omega} \propto E_\omega^2$ in the representative case of the BCN.

We observe in Fig. 3 that the SH signal is concentrated in a pair of arcs, centered on angles $\pm\theta_0$ off the incident direction, with the maximum (peak) intensity located on the axis of the applied magnetic field – i.e., along the nematic director \mathbf{n} – and minimum intensity along the perpendicular axis. Notably, there is a “node” (i.e., SH intensity at the background level) in the center of the images, corresponding to the forward direction ($\theta = 0$). The sharpness of the intensity peaks is due primarily to the focusing effect of the telescope mentioned above; thus, the peaks are artificially narrow [24]. On the other hand, their angular position is clearly defined. The angular dependence recorded here is completely different from the omni-directional distribution of incoherently scattered SH light that is expected from either single or collective molecular orientational fluctuations [6, 7]. In the present experiments, SH scattering from these sources contributes to the nearly flat background level.

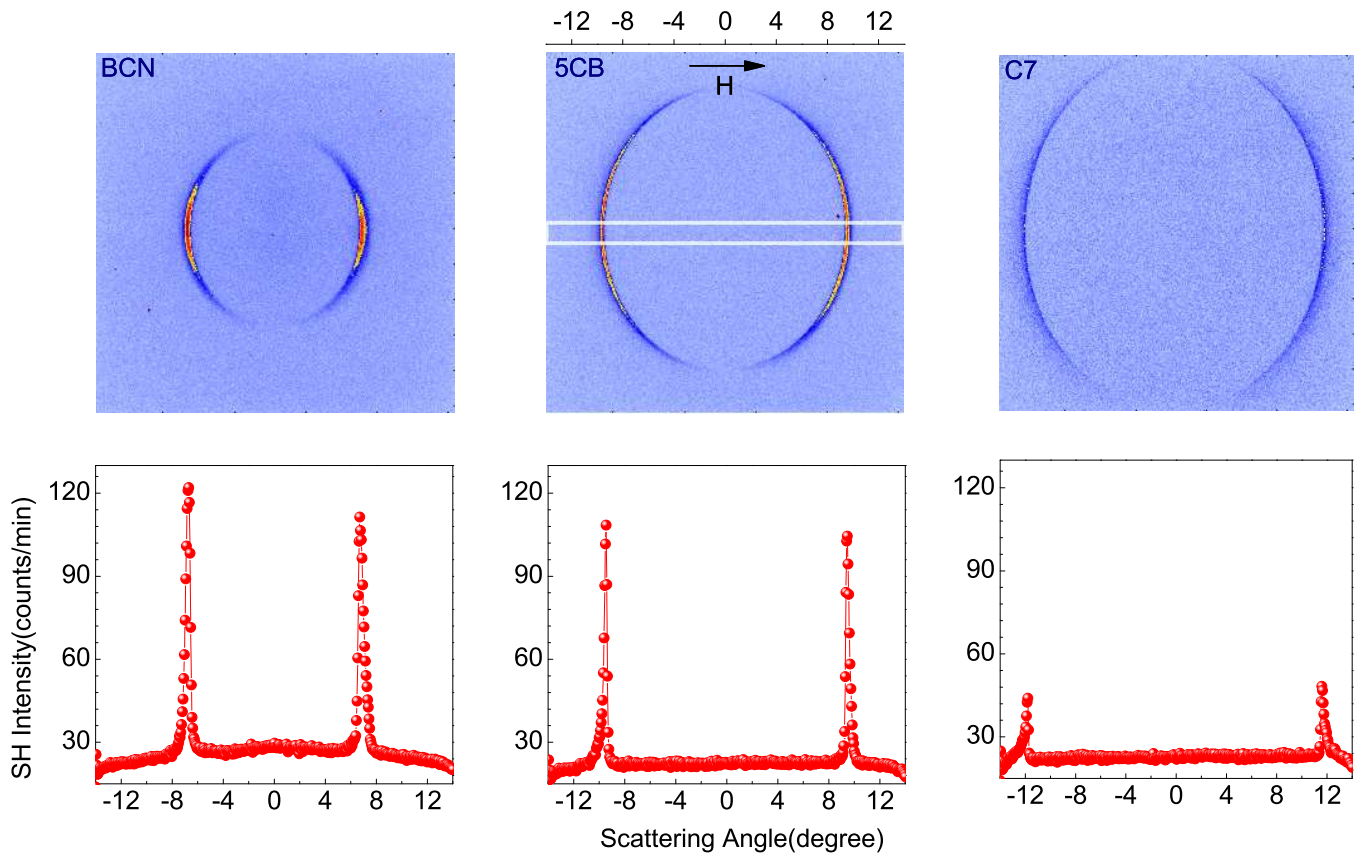


FIG. 3. Representative CCD images of the SH scattering patterns for the $V(\omega) \rightarrow V(2\omega)$ process, recorded at $T_{NI} - T = 2.2^\circ\text{C}$ from (left to right) the BCN, 5CB, and C7 nematic samples. The direction of the applied magnetic field is horizontal, as indicated. Bottom: The SH power plotted as a function of scattering angle (in the scattering plane parallel to \mathbf{H}), after integrating over vertical columns of ± 15 pixels from the horizontal axis through the center. The region used for this average is shown in white outline in the center image, top panel. (As discussed in the text, the peaks are artificially narrowed due to focusing by the telescope optics.)

The data in Fig. 3 (and in Figs. 5, 7 and 8 discussed below) have not been normalized for linear scattering losses or for absorption. However, we determined that absorption in all three materials is negligible at the SH and IR (fundamental) wavelengths. Moreover, at a wavelength (543 nm) close to the SH wavelength (532 nm), the forward linear scattered light intensity integrated over the sensor area is approximately equal for the three samples. As Fig. 3 reveals, at fixed temperature relative to T_{NI} , the peak position shifts from smaller to larger θ in the sequence BCN to 5CB to C7; this shift mirrors the trend in values for the refractive index anisotropies (Δn) for the three nematic compounds. For example, at $T_{NI} - T = 2^\circ\text{C}$, the values are $\Delta n = 0.07$ (BCN) [18], 0.16 (5CB) [25], and 0.24 (C7) [17] at the second harmonic (2ω) frequency. The average (characteristic) peak angle of $\sim 10^\circ$ corresponds to SH scattering from non-centrosymmetric objects of a few μm in size, as calculated using Bragg's law. (The nature of these scatterers will be considered in the next section.) The peak heights are comparable for the bent-core and polar rodlike nematics, while the

signal from the nonpolar compound is much weaker.

The temperature dependence of the SH intensity distribution, for the BCN and the $V(\omega) \rightarrow V(2\omega)$ process, is shown in Fig. 5. The peak position moves out, to larger θ , with decreasing temperature through the nematic phase. Fig. 6 summarizes the dependence of the peak angle θ_0 on T over the nematic range for all three materials studied and for the two processes $V(\omega) \rightarrow V(2\omega)$ and $H(\omega) \rightarrow V(2\omega)$. Interestingly, in all three cases the behavior of θ_0 reflects, at least qualitatively, the temperature dependence of the nematic order parameter S , which decreases continuously toward the first order nematic-isotropic transition, where it is cut off by a discontinuous drop to zero. The values of θ_0 for the $H(\omega) \rightarrow V(2\omega)$ process are slightly higher than for $V(\omega) \rightarrow V(2\omega)$, but as shown in the bottom panels in Fig. 6, the two curves can be matched up with a single scaling factor in each case. We find that a power law fit of the form $\theta_0(T) = \theta_M(T^* - T)^x$ (solid lines in the figure) gives a good description of the temperature dependence, with the following parameter values: $T_{NI} - T^* = 0.32^\circ\text{C}$,

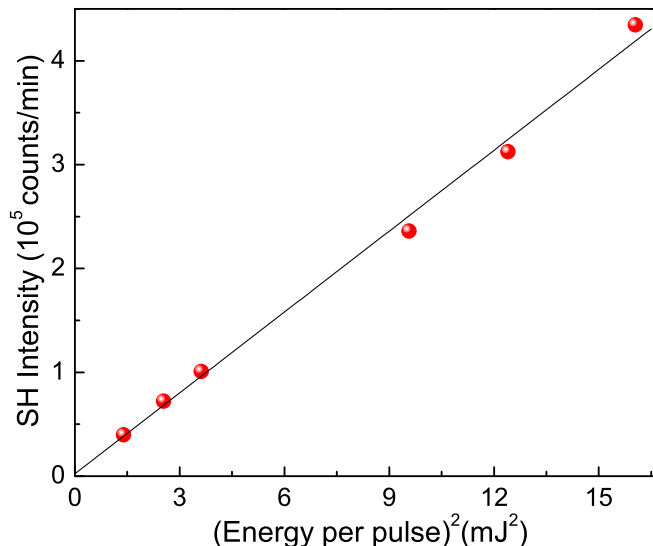


FIG. 4. SH intensity for the BCN sample, integrated over the scattering pattern recorded on the CCD and plotted versus square of the incident IR pulse energy. The solid line is a fit that confirms the expected quadratic relation between the incident and SH powers.

$x = 0.16$ for the BCN; 0.14°C , 0.13 for 5CB; and 0.38°C , 0.10 for C7.

The SH scattering centered at $\pm\theta_0$ diminishes to background level when the samples are heated into the isotropic phase. When the field removed in the nematic phase, the SH signal decreases on a time scale similar to the relaxation of the director alignment. On the other hand, when the sample is cooled from the isotropic to nematic phase in zero field, no SH scattering above the background level is observed; if the field is subsequently applied, the signal rises to similar levels, and peaks are observed at similar angles, as when the sample is cooled in the field from the isotropic state. Thus, the two pathways – cooling after applying field and applying field after cooling – to the same (T, H) in the nematic phase produce essentially equivalent results.

Fig. 7 (top) displays more detailed results for the field dependence of the SH signal for the 5CB sample at $T_{NI} - T = 2.2^\circ\text{C}$ (which are also representative of behavior observed for the other samples). With decreasing field, the SH intensity (integrated vertically over the the area outlined in Fig. 3) first decreases slowly — roughly linearly with H^2 — and then turns over and drops more rapidly below 0.1 T to a value at $H = 0$ that is about 20% of its high field value. The decrease with H is the opposite of what is expected for flexopolar director fluctuations, which, given the positive diamagnetic anisotropy of the studied NLCs, should *increase* in amplitude with decreasing H [6, 7]. The plot in Fig. 7 (bottom), showing the variation with field of the polarized, forward transmitted intensity of a 543 nm laser beam, confirms that the reduction in SH signal upon removal of the field is not due to any significant increase in sample turbidity;

the transmission drops by only 15% when $H \rightarrow 0$.

Finally, the dependence of the SH intensity measured for the three nematics on the incident IR and SH polarizations is presented in Fig. 8; here again the data are plotted versus θ after integrating vertically over the region of the scattering patterns outlined in Fig. 3. For the BCN and 5CB samples, the $V(\omega) \rightarrow V(2\omega)$ and $H(\omega) \rightarrow V(2\omega)$ processes produce peak SH intensities that are much higher than the corresponding processes with $H(2\omega)$ output polarization. Specifically, from the BCN we recorded a weak $H(2\omega)$ signal ($\sim 5\%$ of the $V(2\omega)$ level), while no $H(2\omega)$ output (above background) was detected from 5CB. On the other hand, for the non-polar compound C7 where the overall signal is much weaker, the $H(2\omega)$ output is about 30% of the $V(2\omega)$ level. We conclude that the SH light is predominantly polarized perpendicular to \mathbf{n} (and to the applied magnetic field \mathbf{H}) in the cases of 5CB and the BCN, but is significantly less so for C7.

IV. DISCUSSION

As we have already noted, the angular dependence of the SH scattering in our experiments is completely dif-

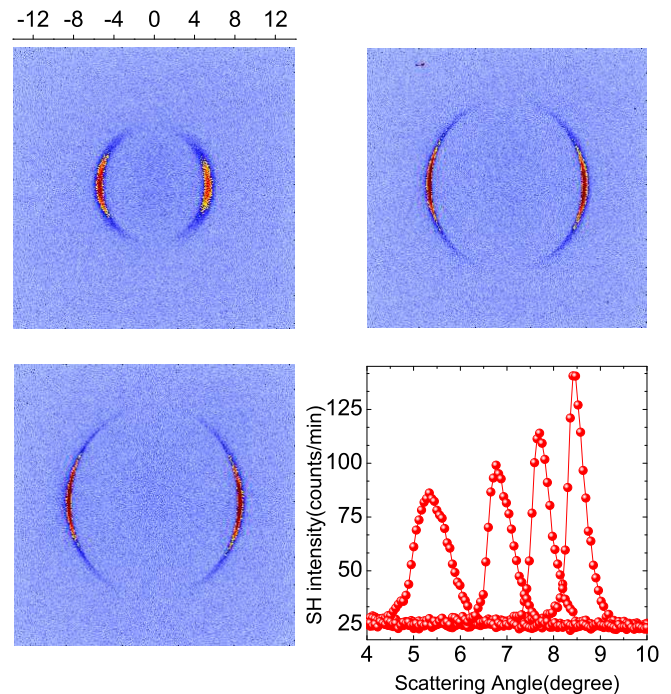


FIG. 5. SH scattering pattern versus temperature in the nematic phase of the BCN for the $V(\omega) \rightarrow V(2\omega)$ process. Upper left, upper right, and lower left: $T_{NI} - T = 0.2, 5.2,$ and 10.2°C , respectively. Lower right: SH power (averaged as described in Fig. 4) versus scattering angle, showing the shift of the peak power to larger scattering angles with decreasing T in the nematic phase ($T_{NI} - T = 0.2, 2.2, 5.2, 10.2^\circ\text{C}$, left to right).

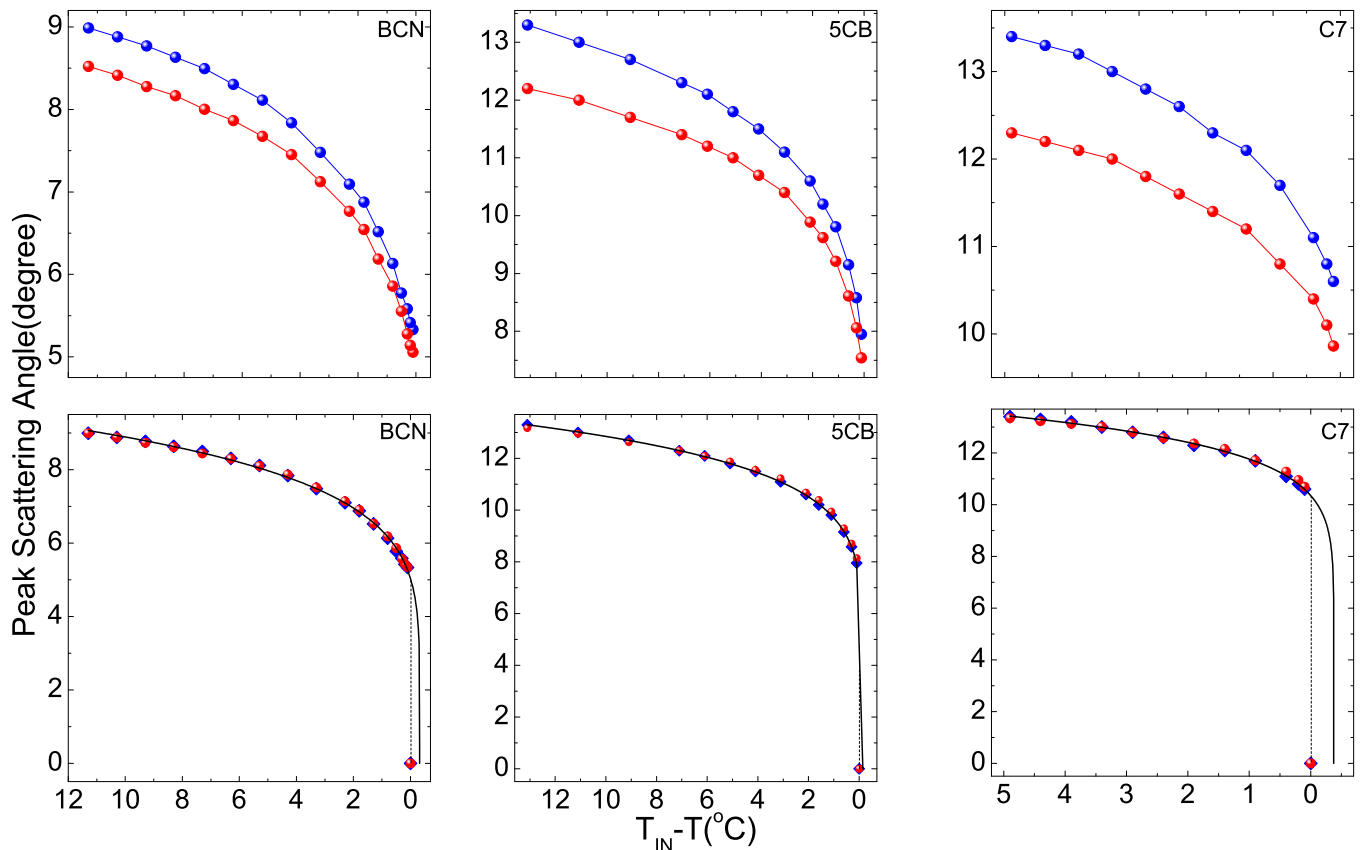


FIG. 6. Peak scattering angle (θ_0) versus temperature for the two processes $V(\omega) \rightarrow V(2\omega)$ (points in red) and $H(\omega) \rightarrow V(2\omega)$ (blue points) for each of the materials studied. Top row: Raw data. Bottom row: Results after rescaling the data for the $V(\omega) \rightarrow V(2\omega)$ process to match the $H(\omega) \rightarrow V(2\omega)$ data. The solid lines are power law fits described in the text, and the dashed vertical lines indicate the first order NI transition temperature. The disappearance of SH signal at T_{NI} is indicated by a single data point in each case.

ferent from that expected from thermal director fluctuations. We can also rule out effects attributable to the fundamental beam itself, including light-induced director reorientation and gradients in the nematic order parameter S caused by local heating (either of which could produce a local electric polarization through flexo- or order electricity). At the pulse energies used, no threshold onset of second harmonic signal was observed. Nor is it plausible that an incident Gaussian beam with \sim mm waist could, without focusing optics, selectively heat domains of a much smaller ($\sim \mu\text{m}$) size that would be consistent with the observed peak SH diffraction angles. In addition, the same SH signal level observed for the two fundamental polarizations along and perpendicular to \mathbf{n} rules out an optical field-induced rotation, which should give dramatically different results for these two cases.

More intriguing is the resemblance of our experimental results to those obtained in SHLS studies [9–12] on colloidal suspensions, in which a layer of non-centrosymmetric material (typically a polar dye) is adsorbed onto the surface of an otherwise centrosymmetric solid particle. In those studies, two key features – the absence of SH intensity scattered in the forward direction

and the presence of symmetric intensity peaks at small angles ($\theta_0 \sim \pm 10^\circ$ for ~ 1 micron spherical particles [10]) – are similar to our results on aligned NLCs.

In fact, this similarity is not merely accidental. Figs. 9(a)–(c) show polarizing microscope images of textures in our 1 mm thick samples taken under the 1.13 T applied field and at a temperature 2.2°C below T_{NI} . The images reveal distributions of micron scale defect loops in the nematic director field \mathbf{n} that appear spontaneously in cooling (at a typical rate of $3^\circ\text{C}/\text{min}$). In the nematic phase the loops appear to form clusters or networks, while in the isotropic phase they completely disappear. Inside and outside the boundaries of the loops, \mathbf{n} is parallel to the applied field \mathbf{H} , but it is distorted across the boundaries. (The distortion tends to depolarize light and thus the boundaries appear darker through parallel polarizer/analyzer). These features are characteristic of *inversion wall loops* – defects in the nematic phase, topologically equivalent to Neel or Bloch walls in ferromagnets [26], in which anti-parallel orientations of the director are separated by a boundary through which \mathbf{n} rotates by π . In the Neel type, \mathbf{n} rotates via splay/bend distortion, thus generating a flexoelectric polarization [1] and

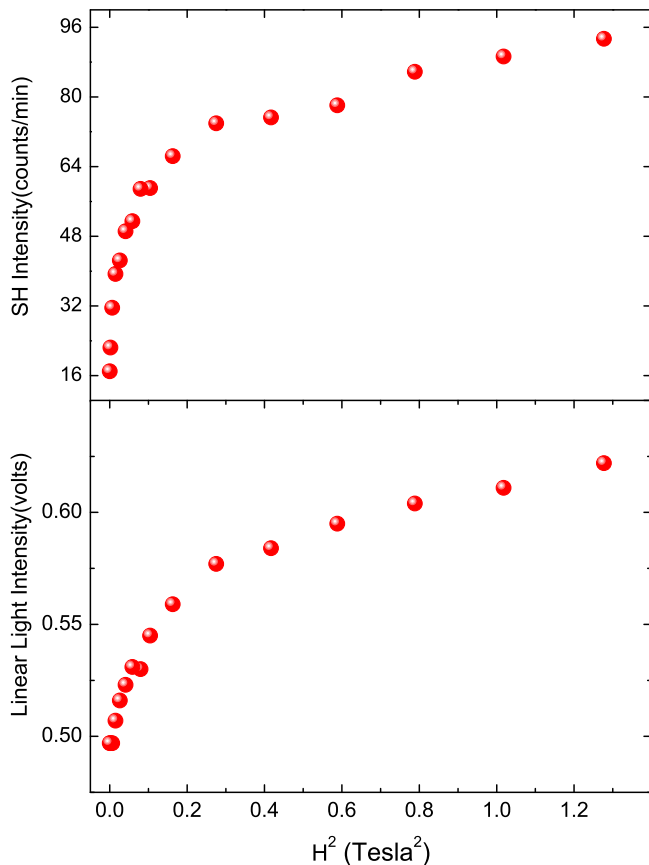


FIG. 7. Top: Integrated SH intensity versus applied field squared for the 5CB sample. Bottom: Linear light transmission (forward direction) versus H^2 for a 543 nm laser beam.

non-centrosymmetry in the boundary region; the nematic remains centrosymmetric in the undistorted regions on either side. (By contrast, the Bloch type involves a pure twist in \mathbf{n} .) Hence one can expect that basic features of the SHLS pattern from the defect loops should indeed resemble those from a dispersion of small centrosymmetric particles with non-centrosymmetric surface layers.

The director configuration in Neel inversion loops has been studied in detail by phase-contrast TEM, SEM, and AFM performed on polymer nematic films [27, 28, 30]. Fig. 10(a) depicts the experimentally observed configuration [27]: The solid lines represent trajectories of \mathbf{n} (indicated by arrows), while the dashed line traces a loop of inversion points in the plane of the figure. The loop boundary contains a mixture of “splay-bend” distortions in \mathbf{n} (corresponding to the cusp-like trajectories on the left and right sides of the loop) and “bend-splay” distortions (corresponding to the hairpin-like trajectories on the top and bottom sides). In thick samples, the loops extend into a cylinder-like structures, which may relax into an undistorted state in the bulk or terminate at a boundary surface.

Inversion walls and loops are typically generated by electric or magnetic fields applied normal to the orienta-

tion of \mathbf{n} in nematics with positive dielectric or diamagnetic anisotropy [26], as in the case of the studies cited above, or they may be induced by flow as demonstrated, for example, in microfluidic channels [29]. A combination of flow patterns that tends to randomize the orientation of \mathbf{n} and applied field can produce large populations of these defects. In our relatively thick samples, thermal gradients cause convective flows at the isotropic–nematic transition, which are readily observed in the microscope and which have a randomizing effect on the incipient nematic domains (e.g., through the coupling of molecular translations and rotations). In a significant fraction of these domains, \mathbf{n} is orthogonal to the applied field \mathbf{H} , and the degeneracy in magnetic energy for $\mathbf{n} \parallel \mathbf{H}$ and $-\mathbf{n} \parallel \mathbf{H}$ (i.e., the equivalence of \mathbf{n} and $-\mathbf{n}$ in the nematic state) leads to the spontaneous formation of inversion walls and (in thicker samples or at higher flow rates [29]) inversion loops. The plane of the loops in Fig. 9 is parallel to the direction of \mathbf{H} , which is consistent with the Neel-type wall structure in Fig. 10a.

Since the minimum nematic free energy (for positive diamagnetic anisotropy) corresponds to uniform \mathbf{n} , inversion walls forming at the isotropic–nematic transition under the field are unstable, and should anneal out with time. However, as pointed out by Helfrich [26] and observed by different groups [31–34], inversion walls may be pinned and stabilized at solid surfaces bounding the nematic sample, with characteristic parameters – wall thickness, penetration length into the bulk, and, in the case of loops, the loop diameter – determined by an appropriate combination of surface and bulk contributions to the free energy. In our samples, the loops were most clearly resolved when the microscope was focused at the boundary surfaces of the sample cells, and the loops are stable and immobile for at least several hours at fixed temperature; no effect of annealing over this time period was noticeable. These observations clearly point to surface pinning of the loops. Since we did not observe any significant surface memory effects when cycling the samples through the N-I transition in the field, the most likely scenario is that some fraction of loops are randomly pinned at sites on the surfaces after first being generated in the sample bulk.

The size distribution of the loops in Fig. 9 is fairly narrow, with the characteristic diameter being 3–4 μm . We can rationalize this value as follows. We assume that the width ξ of the wall (region where \mathbf{n} varies rapidly) is set by the conditions of its formation in the bulk – i.e., $\xi = \sqrt{K/\Delta\chi H^2}$ [26], where where $\Delta\chi \simeq 5 \times 10^{-7}$ cgs is the typical diamagnetic susceptibility anisotropy of the nematic and $K \simeq 5 \times 10^{-7}$ dyne is the typical Frank elastic constant. This gives $\xi \simeq 0.9 \mu\text{m}$ for the applied field of $H = 11300$ G. Next we suppose that one side or position along the wall becomes pinned at a boundary surface; in this case, the loop can still shrink to a minimum diameter D in order to reduce its bulk energy cost. As indicated in Fig. 11 (discussed below), this diameter (for near overlap of the distorted regions of the walls on

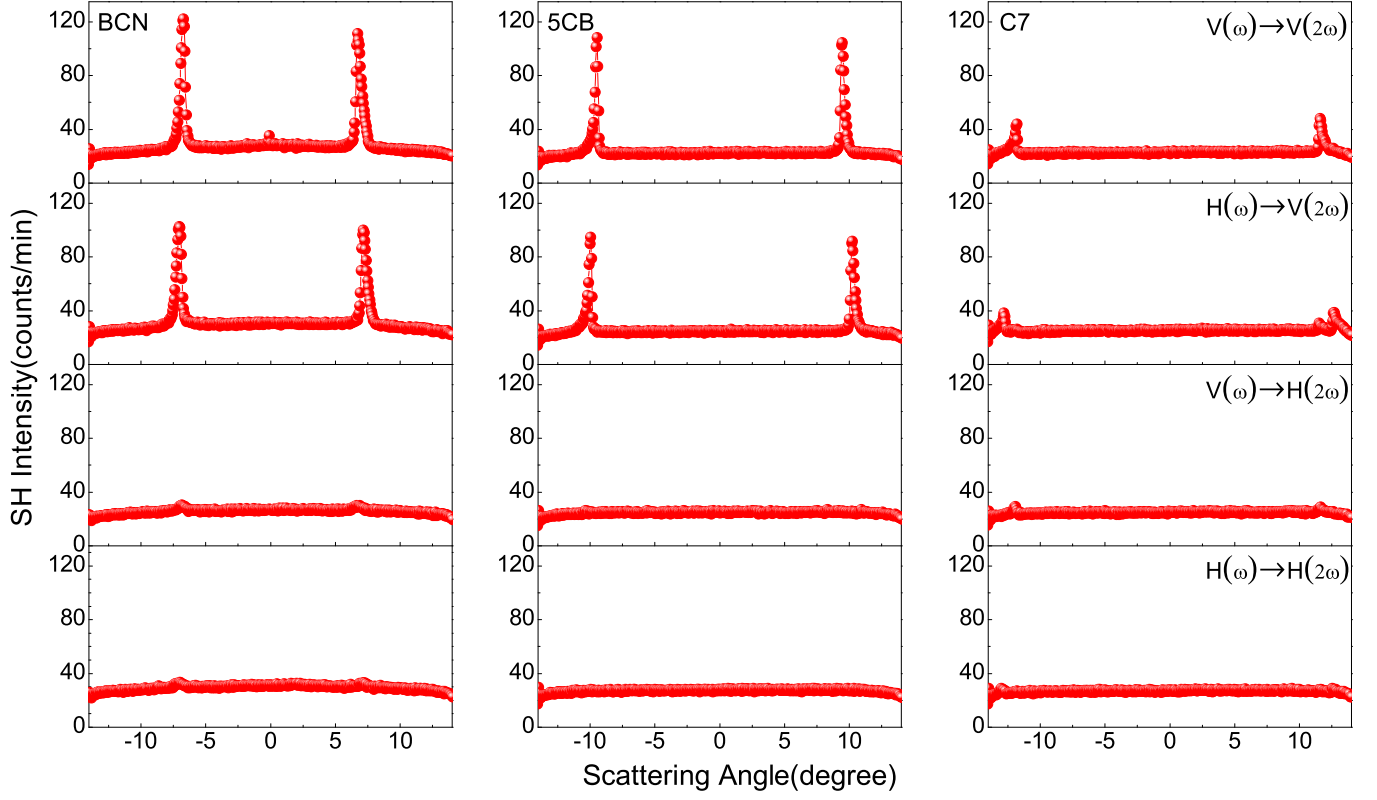


FIG. 8. Dependence of the SH scattering on the fundamental (ω) and SH (2ω) polarizations for $T_{NI} - T = 2.2^\circ\text{C}$.

opposite sides of the loop) corresponds to $D \simeq 4\xi$. Using our estimate of ξ , we get $D \simeq 3.6 \mu\text{m}$, in good agreement with the observed diameter.

In order to develop the connection between the inversion loops and SHLS from our samples, we consider the flexoelectric polarization \mathbf{P}_f induced by distortion in \mathbf{n} [1]:

$$\mathbf{P}_f = e_1 \mathbf{n} (\nabla \cdot \mathbf{n}) + e_3 (\nabla \times \mathbf{n}) \times \mathbf{n} \quad (1)$$

Here e_1 and e_3 are material-dependent flexoelectric coefficients for splay and bend distortions, respectively. The effective second order nonlinear susceptibility $\chi_{eff}^{(2)}$ may be written as a contraction of \mathbf{P}_f with the third rank susceptibility $\chi^{(3)}$ (which is permitted in a medium of arbitrary symmetry) [7, 35],

$$\chi_{eff}^{(2)} = \chi^{(3)} \cdot \mathbf{P}_f / \epsilon_0 \bar{\chi}_e \quad (2)$$

where $\bar{\chi}_e$ denotes the average dielectric susceptibility of the NLC (for simplicity, we ignore the anisotropy in χ_e due to nematic order). Symmetry of the NLC under $\mathbf{n} \rightarrow -\mathbf{n}$ requires that all components of $\chi^{(3)} = \chi_{ijkl}^{(3)}$ with a non-recurring index vanish [36]. The key quantity determining the properties of the SHLS is the induced

nonlinear dipole moment given by

$$\begin{aligned} \mathbf{p}_{2\omega}(\mathbf{q}) &= \int_V \mathbf{P}_{2\omega}(\mathbf{r}') \exp(i\mathbf{q} \cdot \mathbf{r}') dV' \\ &= E_0^2 \int_V \chi_{eff}^{(2)}(\mathbf{r}') : \hat{\mathbf{e}}_\omega \hat{\mathbf{e}}_\omega \exp(i\mathbf{q} \cdot \mathbf{r}') dV' \quad (3) \end{aligned}$$

In this expression, E_0 is the amplitude of the fundamental field, $\hat{\mathbf{e}}_\omega$ is the polarization of the fundamental field, $\mathbf{q} = \mathbf{k}_{2\omega} - 2\mathbf{k}_\omega$ is the SH scattering vector, and the integral is taken over the inversion wall loop.

Next, to describe the director field associated with the splay-bend and bend-splay inversions, we use the coordinate system specified in Fig. 10 and assume (again for simplicity) a single Frank elastic constant, $K_1 = K_3 = K$. Then $\mathbf{n} = \sin \phi \hat{\mathbf{x}} + \cos \phi \hat{\mathbf{z}}$ and the orientational free energy density in field \mathbf{H} is:

$$f(\phi) = \frac{1}{2} K (\nabla \phi)^2 - \frac{1}{2} \Delta \chi H^2 \cos^2 \phi \quad (4)$$

To avoid unnecessary mathematical complexity, we consider separately the variation of ϕ in the ‘‘splay-bend’’ regions of the loop (left and right sides in Fig. 10a) and in the ‘‘bend-splay’’ regions (top and bottom sides). Then the following expressions apply in the two cases [26]:

$$\begin{aligned} \phi^{sb}(z) &= 2 \tan^{-1} [\exp(\pm z/\xi)] \\ \phi^{bs}(x) &= 2 \tan^{-1} [\exp(\pm x/\xi)] \quad (5) \end{aligned}$$

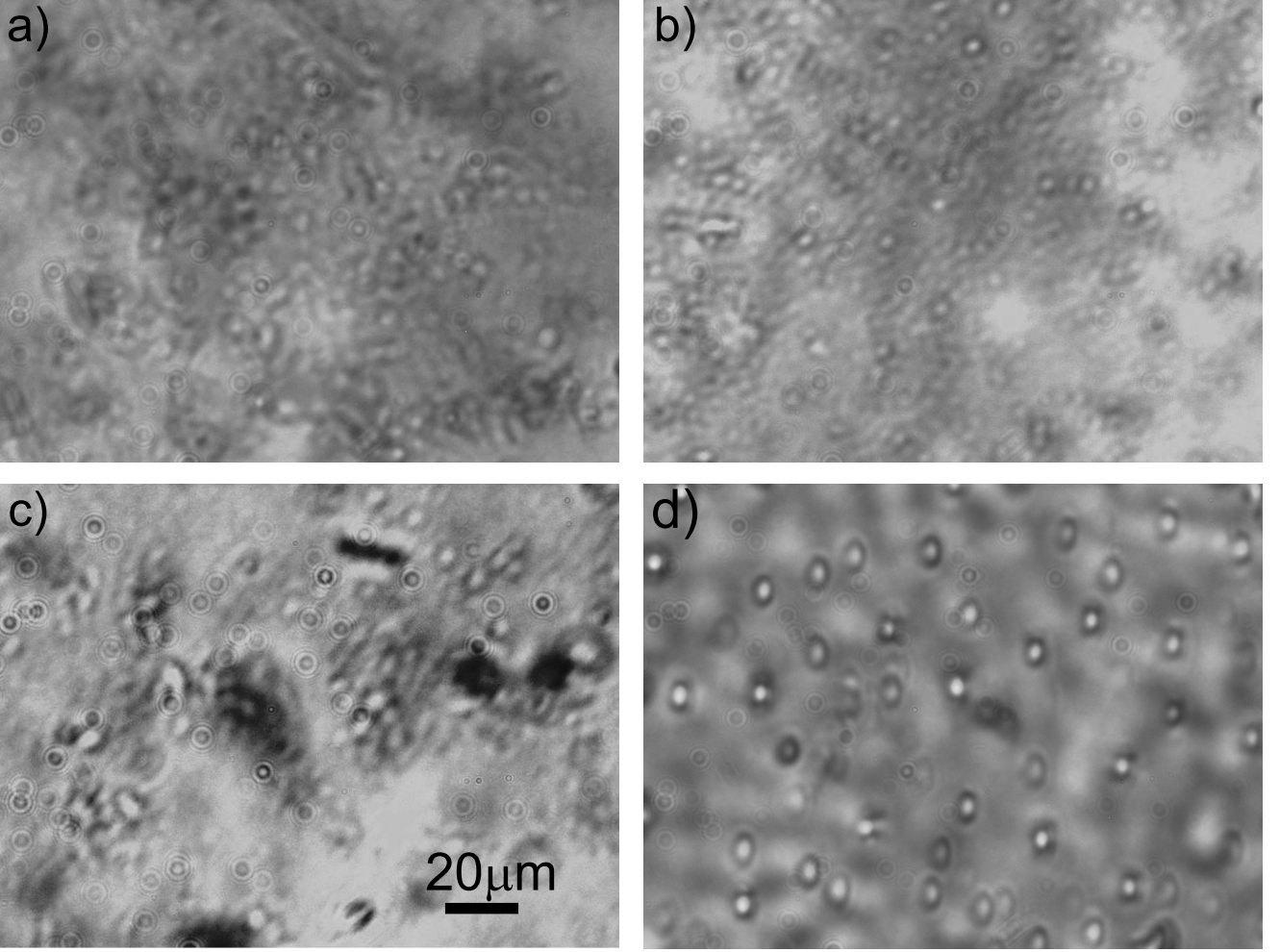


FIG. 9. Polarizing microscope images of metastable inversion wall loops in the three different nematic liquid crystals studied: (a) 1 mm thick 5CB, (b) 1 mm thick C7, (c) 1 mm thick BCN, (d) 0.1 mm thick 5CB. The images were recorded after cooling the samples from the isotropic state to a temperature 2.2°C below the isotropic–nematic transition under a constant 1.13 T magnetic field, directed approximately left to right in the figure. The microscope was focused on a plane just below the sample–substrate interface where the features of the loops are sharpest; the resolution is limited due to the thickness of the samples. The images are rendered in gray scale to facilitate comparison.

Here the superscripts *sb* and *bs* refer to the splay-bend (left and right) and bend-splay (top and bottom) sides of the inversion loop in Fig. 10a, while the “+” or “−” sign applies to the left and top or right and bottom sides, respectively. The points $z = 0$ or $x = 0$ correspond to the center of the inversion wall (where $\mathbf{n} \perp \mathbf{H}$) in all cases. The parameter $\xi = \sqrt{K/\Delta\chi H^2}$ gives the characteristic width of the inversion wall. Then, from Eq. (1), we obtain the following expressions for \mathbf{P}_f :

$$\begin{aligned} \mathbf{P}_f^{sb}(z) &= \pm \frac{1}{2\xi \cosh(z/\xi)} \{ [e_1 \sin^2 \phi(z) - e_3 \cos^2 \phi(z)] \hat{\mathbf{x}} \\ &\quad + (e_1 + e_3) \sin \phi(z) \cos \phi(z) \hat{\mathbf{z}} \} \\ \mathbf{P}_f^{bs}(x) &= \pm \frac{1}{2\xi \cosh(x/\xi)} \{ (e_3 - e_1) \sin \phi(x) \cos \phi(x) \hat{\mathbf{x}} \\ &\quad - [e_1 \cos^2 \phi(x) + e_3 \sin^2 \phi(x)] \hat{\mathbf{z}} \} \end{aligned} \quad (6)$$

The “+” and “−” signs again refer the inversion walls on opposite sides of the loop.

We consider several properties related to the above expressions for \mathbf{P}_f :

1. The induced nonlinear polarization $\mathbf{P}_{2\omega}$ in Eq. (3) has the same orientation as \mathbf{P}_f ; in particular $\mathbf{P}_{2\omega}^{sb} \parallel \mathbf{P}_f^{sb}$ and $\mathbf{P}_{2\omega}^{bs} \parallel \mathbf{P}_f^{bs}$. This follows from the fact that $\chi^{(3)}$ in Eq. (2) is non-zero only if each index is recurring. Thus, $\mathbf{P}_{2\omega} = (E_0^2/\epsilon_0 \bar{\chi}_e) \chi^{(3)} : \mathbf{P}_f \hat{\mathbf{e}}_\omega \hat{\mathbf{e}}_\omega$ implies $P_{2\omega,i} = (E_0^2/\epsilon_0 \bar{\chi}_e) \chi_{iijj}^{(3)} P_{f,i} e_{\omega,j} e_{\omega,j}$.
2. If e_1 and e_3 are similar in magnitude but opposite in sign ($e_1 \simeq -e_3$), the integrated \mathbf{P}_f across the inversion wall produces an effective surface dipole density, which has a large x component in the splay-

bend regions yet tends to vanish in the bend-splay regions. Additionally, the direction of \mathbf{P}_f^{sb} is opposite on the left and right sides of the loop in Fig. 10, while its magnitude is similar. This is illustrated in Fig. 11, and also by the map of polarization vectors shown in Fig. 10b, for the case $e_3 = -e_1$ (the ‘‘one coefficient’’ approximation often used in theoretical analyses of the effect of flexoelectricity on defect structures in NLCs [16]). Experimentally, the values of the flexoelectric coefficients are still rather uncertain, even for standard nematics. Different reports have, for example, given the sum $e_1 + e_3$ as either negative or positive [37] in 5CB.

- Points 1 and 2 imply that $\mathbf{P}_{2\omega}^{sb}$ has opposite directions (but equal magnitudes) on the left and right sides of the loop (along \mathbf{H}) provided $e_1 \simeq -e_3$. They also imply that the integral of $\mathbf{P}_{2\omega}^{bs}$ over the wall thickness on top and bottom of the loop tends to vanish. This results in an average induced nonlinear polarization normal to \mathbf{H} that points in opposite directions on opposite sides of the loop (Fig. 10c).

Let us compare our SHLS results to the proposed model with the properties enumerated above:

Nodal line in SH scattering for $\mathbf{q} \perp \mathbf{H}$: We refer to the coordinate system in Fig. 10, and consider for simplicity a circular loop with diameter D in the x - z plane at $y = y_0$ with thickness Δy about y_0 . The contribution to the integral in Eq. (3) over the inversion walls on the left and right sides of the inversion loop (i.e., along z with $x = 0$) is

$$e^{iq_y y_0} \Delta x \Delta y \int dz \left\{ \mathbf{P}_{2\omega}^{sb}(-D/2 + z) e^{iq_z(-D/2+z)} + \mathbf{P}_{2\omega}^{sb}(D/2 + z) e^{iq_z(D/2+z)} \right\}$$

where $\mathbf{P}_{2\omega}^{sb}$ is given by the combination of the first expression in Eq. (6) and Eq. (2). The integral is taken over the characteristic thickness of the wall (i.e., the thickness ξ over which ϕ varies significantly) with the origin at the center of the wall. Similarly, for the top and bottom sides (along x with $z = 0$), the contribution to the integral in Eq. (3) is

$$e^{iq_y y_0} \Delta y \Delta z \int dx \left\{ \mathbf{P}_{2\omega}^{bs}(-D/2 + x) e^{iq_x(-D/2+x)} + \mathbf{P}_{2\omega}^{bs}(D/2 + x) e^{iq_x(D/2+x)} \right\}$$

where $\mathbf{P}_{2\omega}^{bs}$ is given by the combination of the second expression in Eq. (6) and Eq. (2). Now for $\mathbf{q} \perp \mathbf{H}$ (i.e., $q_z = 0$), the first integral above tends to zero, since by points 1 – 3 above, $\mathbf{P}_{2\omega}^{sb}(D/2 + z) \simeq -\mathbf{P}_{2\omega}^{sb}(-D/2 + z)$ in the integrand. On the other hand, for the second integral if $q_x \ll 2\pi/\xi$ (i.e., for small angles where $\sin \theta \ll 1$), we may set $\exp(iq_x x) = 1$ to lowest order, and then the two terms in the integral are proportional

to $\int_{-\xi}^{\xi} dx \mathbf{P}_{2\omega}^{bs}(\pm D/2 + x)$, which tend to zero according to point 3. Thus, provided $e_1 \simeq -e_3$, we expect minimum SH scattering when $q_z = 0$. However, the argument for a node *specifically in the forward direction* ($\theta = 0$) requires only that $\mathbf{P}_{2\omega}^{sb}$ and $\mathbf{P}_{2\omega}^{bs}$ are equal in magnitude but oppositely directed on the opposite sides (left and right, top and bottom) of the inversion loop. This is a special case of a general symmetry condition for a forward node, which was discussed in the SHLS studies on colloidal systems [12]: Such a node occurs if the nonlinear polarization associated with the individual scatterers possesses π -rotation symmetry about the wavevector \mathbf{k}_ω of the incident (fundamental) light.

Small angle peaks for $\mathbf{q} \parallel \mathbf{H}$: Here we consider $q \simeq q_z$ and $q_x \simeq 0$, corresponding to the observed peaks. For the same reasons just given, the x integral above tends to zero. However, the opposing signs (but equal magnitudes) of $\mathbf{P}_{2\omega}^{sb}$ on opposite sides of the inversion loop in Fig. 10(c) along the z axis imply that the z integral above (and thus Eq. (3)) will have a peak when the two terms in the integral are out of phase. This gives a relation between the angular position of the peak and the loop diameter D of the form $D \sin \theta_0 \simeq \lambda_{2\omega}$, where the ‘‘ \simeq ’’ sign indicates accuracy up to a factor of order unity. (A more exact condition could be obtained numerically given knowledge of the quantities entering into Eq. (3), including details on the shape of the inversion loops.) Taking typical $\theta_0 = 10^\circ$ (Fig. 3), we estimate $D \simeq 3.2 \mu m$, in good agreement with the images of the loops in Fig. 9.

Polarization selectivity: From the above discussion, the SH scattering peaks come mainly from the contribution of $\mathbf{P}_{2\omega}^{sb}$, which is along the x axis in Fig. 10. Thus, the main component of the induced nonlinear dipole moment $\mathbf{p}_{2\omega}$ is parallel to $\hat{\mathbf{x}}$. Since the wavevector $\hat{\mathbf{k}}_{2\omega}$ corresponding to the observed small angle peaks, lies in the $y - z$ plane, the transverse component of $\mathbf{p}_{2\omega}$ and thus the SH field are predominantly along $\hat{\mathbf{x}}$, which corresponds to $V(2\omega)$ polarization, as indeed observed in our NLC samples [38]. For the C7 sample, however, the $H(2\omega)$ output is not completely negligible compared to the $V(2\omega)$ component. This indicates that the model described above may not apply, perhaps due to the importance of a quadrupolar contribution to flexoelectricity in this NLC (see discussion below).

The polarization selectivity of SH scattering from the inversion loops in NLCs differs from the colloidal system referenced above. In the latter case, the distribution of dipole moments on the surfaces of the spherical particles is radial. Although $\mathbf{P}_{2\omega}$ is still oppositely directed on opposite sides of the particles (leading to a forward node in the scattering pattern), the predicted and measured SH output is polarized predominantly parallel to the scattering plane, corresponding to $H(2\omega)$ rather than $V(2\omega)$ output.

Field dependence of SH signal: To account for the behavior of the SH signal with field shown in Fig. 7, we consider two aspects of the inversion loop structure. If

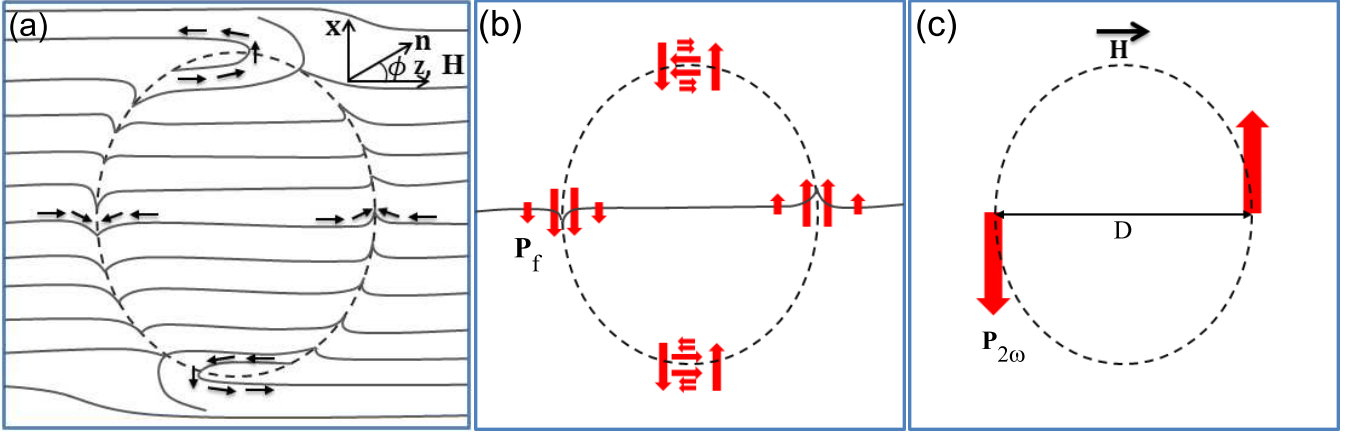


FIG. 10. Left panel(a): Schematic illustration of an inversion wall loop in an aligned nematic (after ref. [27]). The dashed oval traces the center of the wall (points where the angle ϕ of the director \mathbf{n} reaches $\pi/2$ with respect to the equilibrium orientations $\phi = 0, \pi$ along the aligning field \mathbf{H}). The left and right sides of the loop along the z direction contain a splay-dominated mixture of splay-bend director distortions (labeled *sb* in the text), while the top and bottom sides along the x direction are richer in bend (and are labeled *bs* in the text). Arrows indicate the rotation of the \mathbf{n} through the wall. Middle panel (b): Qualitative map of flexoelectric polarization in the *sb* and *bs* regions of the loop for the specific case of equal and opposite splay and bend flexoelectric coefficients, $e_1 = -e_3$. (The results of a detailed calculation are presented in Fig. 11.) Right panel (c): Map of the average induced nonlinear polarization resulting from the distribution of flexoelectric polarization in (b). Note the opposite orientations of $\mathbf{P}_{2\omega}$ across the diameter D .

the three-dimensional structure is cylinder-like, extending from the sample surfaces partially into the bulk, then for $\Delta\chi > 0$, the field would tend to align the tube axes normal to \mathbf{H} . This creates the possibility of coherent SH light being generated along the length of tubes oriented perpendicular to \mathbf{H} and parallel to \mathbf{k}_ω , enhancing the SH signal. The initial rapid rise of the signal with H^2 followed by a roll-off can then be explained by saturation in tube alignment, which could occur at relatively low field since the tube contains a large number of molecules.

The slower, linear in H^2 rise in SH intensity at higher fields can be understood from the field dependence of the characteristic width ξ of the inversion walls. In the simple model described above, $\xi^2 \propto H^2$ and then using $I_{2\omega} \sim p_{2\omega}^2 \sim P_f^2 \sim \xi^{-2}$ (see Eq. (6)), we get $I_{2\omega} \sim H^2$.

Dependence of SH signal on sample thickness: So far we have made only limited measurements of the SHLS intensity for different sample thicknesses. In a 0.1 mm thick samples, exposed to the same experimental conditions as our 1 mm samples, we find the angular distribution of SHLS is similar to the arc-like patterns in Fig. 3 but the overall signal is ~ 100 times weaker. The somewhat surprising result that the signal does not simply scale with thickness can be attributed to a reduction in the density of the inversion loops observed in the thinner cells. As Fig. 9(d) reveals, the number of loops pinned at the surfaces in the 0.1 mm sample of 5CB is substantially lower than in the 1 mm sample, over an equal surface area. We can explain this difference as follows: Thermal gradients are significantly diminished in the narrower cell, resulting in reduced (and more confined) convective flow as the sample passes through the isotropic-nematic transition.

According to our earlier discussion, this implies a lower population of inversion loops generated in the presence of the magnetic field [39]. In addition, if the loops do not extend as far into the bulk in thinner samples, the SH intensity would be further reduced.

Temperature dependence of θ_0 : As the temperature is decreased in the nematic phase, the orientational elastic constants and the diamagnetic anisotropy both increase; thus the elastic and field energies in the distorted regions of the inversion wall loop increase at lower temperature. To offset this increase, the dimensions of the loop can shrink, producing an increase in the angle θ_0 corresponding to the peak in SH scattering. Strictly speaking, this argument applies to the bulk; the diameter of the loop at the surface may not change as much. A direct confirmation of changing loop size requires imaging with better three-dimensional resolution than our microscope is presently capable of.

Material dependence of θ_0 and peak SH power: At fixed temperature relative to T_{NI} and fixed H , the value of θ_0 increases in the order of materials BCN \rightarrow 5CB \rightarrow C7 (Fig. 3), which also corresponds to the order of increasing refractive index anisotropy Δn . For the former two, the magnitude of the diamagnetic anisotropy correlates with Δn , so we expect a lower inversion loop energy in fixed field, and hence a higher D and lower θ_0 , in the BCN. Assuming the magnitudes of Δn and $\Delta\chi$ are correlated for C7, this material would be expected to show the largest θ_0 , as observed. Unfortunately, we are not aware of any measurements of $\Delta\chi$ for C7.

The SH signal recorded from the nonpolar compound

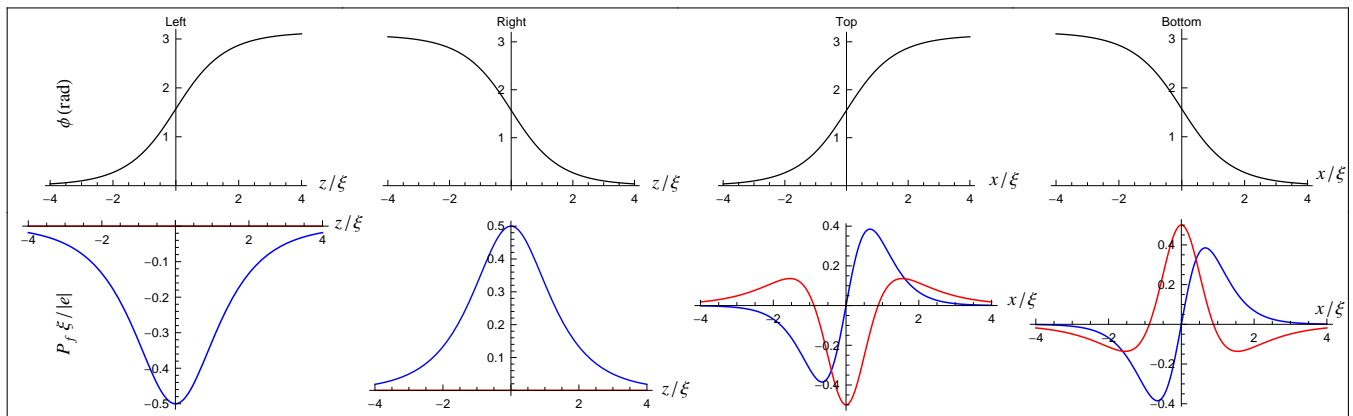


FIG. 11. Top row: Angle of the director ϕ (relative to the applied field \mathbf{H}) plotted as a function of z/ξ through the left and right sides of the inversion loop (sb regions), and as a function of x/ξ through the top and bottom sides (bs regions). The plots are based on Eq. (6) in the text. The x and z directions are defined in Fig. 9; the origin corresponds to the center of the inversion wall in each case. Bottom row: Corresponding components of the flexoelectric polarization plotted as a function of position for the case $e_1 = -e_3$, according to Eq. (6) in the text. P_x^f (P_z^f) is shown as a blue (red) curve.

C7 is weaker than the other materials. In nonpolar mesogens, a polarization induced by distortion in \mathbf{n} can arise due to a quadrupolar flexoelectric effect [40]. Although one would expect this to be of higher order, it has in fact been reported to have a similar order of magnitude as dipolar flexoelectricity [41].

The signals detected from the polar rodlike mesogen (5CB) and the BCN are comparable. Based on the model described above, one might conclude that the flexoelectric coefficients should have the same order of magnitude for the two compounds. This conclusion assumes the density of inversion loops is also comparable in the two nematics, which is not clear from the images in Fig. 9. However, when thin samples of the BCN are subjected to direct mechanical flexure, the induced polarization current is found to be several orders of magnitude higher than for standard nematics like 5CB [22]. As was pointed out in [22], the large polarization current cannot be explained by the conventional molecular statistical theory of flexoelectricity [42] together with the phenomenological expression in Eq. (1). Instead, it may arise from the response of the unconventional cybotactic nanostructure [19] of the BCN to mechanical stresses.

V. CONCLUSION AND OUTLOOK

We have described small angle, second-harmonic light scattering studies performed on magnetically-aligned samples of various NLCs. The angular distribution of scattered SH power can be clearly related to the presence of inversion wall loops – defects in which two regions of uniform nematic director are separated by a π inversion wall – and specifically to the flexoelectric polarization (non-centrosymmetry) associated with the distortion of \mathbf{n} in the walls. Our results are consistent with the relation $e_1 \simeq -e_3$ between the flexoelectric coefficients in quite

different nematic materials, a rod-like and a bent-core compound. This is at present a qualitative conclusion, but one which we hope stimulate further development of the SHLS approach.

Indeed, there are several interesting directions for such development, which could enable more quantitative study of flexoelectric properties. Various technologies to pattern periodic one- and two-dimensional arrays of defects in the nematic director field have been demonstrated recently. These include optical patterning by light-induced reorientation of \mathbf{n} [43], patterning of alignment layers by AFM [44] or by photo-lithography [45], and the use of controlled flows in microfluidic channels to produce parallel arrays of disclination walls [29]. In such patterned arrays, where spatial periods of $\sim 10 \mu\text{m}$ are currently achievable over $\sim \text{mm}$ dimensions, a precise spatially-periodic variation of the flexoelectric polarization $\mathbf{P}_f(\mathbf{r})$ in terms of parameters e_1 and e_3 would be prescribed, and could then be tailored to optimally define the angular distribution of SH light. Alternatively, while with our present set-up we are not able to detect the signal from single defects, there are straightforward means by which the SH sensitivity could be improved [47], potentially obviating the need to produce controlled arrays or to obtain high densities of spontaneously formed defects. In either case, true quantitative comparisons of the flexoelectric parameters among different nematics would still require separate measurements of the relevant components of $\chi^{(3)}$, but these can be carried out by third harmonic generation [46], for example.

In a more general sense, SHLS provides a potentially useful approach to investigate, on optical length scales, the polar structure of topological defects in liquid crystalline materials.

VI. ACKNOWLEDGMENTS

We are very grateful to Dr. E. Korblova (Department of Chemistry, University of Colorado, Boulder) for pro-

viding the nonpolar nematic compound C7, and to Dr. P. K. Challa for assistance in setting up our experiments. This research was supported by the NSF under grants DMR-0964765 and DMR-1307674.

-
- [1] R. B. Meyer, *Piezoelectric Effects in Liquid Crystals*, Phys. Rev. Lett. **22**, 918 (1969).
- [2] See, for example, the review of “bow”-shaped or bent-core liquid crystals by H. Takezoe and Y. Takanishi, *Bent-Core Liquid Crystals: Their Mysterious and Attractive World*, Jpn. J. Appl. Phys. **45**, 597 (2006).
- [3] M. Cestari et al, *Phase behavior and properties of the liquid-crystal dimer 1'',7''-bis(4-cyanobiphenyl-4'-yl) heptane: A twist-bend nematic liquid crystal*, Phys. Rev. E **84**, 031704 (2011).
- [4] M. B. Feller, W. Chen, and Y. R. Shen, *Investigation of surface-induced alignment of liquid-crystal molecules by optical second-harmonic generation*, Phys. Rev. A **43**, 6778 (1991); Y. R. Shen, *Studies of liquid crystal monolayers and films by optical second harmonic generation*, Liq. Cryst. **5**, 635 (1989).
- [5] S.-J. Gu, S. K. Saha, and G. K. Wong, *Flexoelectric Induced Second-Harmonic Generation in a Nematic Liquid Crystal*, Mol. Cryst. Liq. Cryst. **69**, 287 (1981).
- [6] M. Copic and T. Ovsenik, *Second-Harmonic Scattering on Orientational Fluctuations in Nematics*, Europhys. Lett. **24**, 93 (1993).
- [7] S. H. Hong, J. C. Williams, R. J. Twieg, A. Jakli, J. Gleeson, S. Sprunt, and B. Ellman, *Second-harmonic generation in a bent-core nematic liquid crystal*, Phys. Rev. E **82**, 041710 (2010).
- [8] S. Chandrasekhar, *Liquid Crystals*, second edition (Cambridge University Press, Cambridge, England, 1992), Chapter 3.
- [9] J. I. Dadap, J. Shan, K. B. Eisentah, and T. F. Heinz, *Second-Harmonic Rayleigh Scattering from a Sphere of Centrosymmetric Material*, Phys. Rev. Lett. **83**, 4045 (1999).
- [10] N. Yang, W. E. Angerer, and A. G. Yodh, *Angle-Resolved Second-Harmonic Light Scattering from Colloidal Particles*, Phys. Rev. Lett. **87**, 103902 (2001).
- [11] J. I. Dadap, J. Shan, and T. F. Heinz, *Theory of optical second-harmonic generation from a sphere of centrosymmetric material: small-particle limit*, J. Opt. Soc. Am. **21**, 1328 (2004).
- [12] J. Shan, J. I. Dadap, I. Stiopkin, G. A. Reider, and T. F. Heinz, *Experimental study of optical second-harmonic scattering from spherical nanoparticles*, Phys. Rev. A **73**, 023819 (2006).
- [13] G. P. Alexander and J. M. Yeomans, *Flexoelectric blue phases*, Phys. Rev. Lett. **99**, 067801 (2007).
- [14] R. Castles, S. M. Morris, E. M. Terentjev, and H. J. Coles, *Thermodynamically stable blue phases*, Phys. Rev. Lett. **104**, 157801 (2010).
- [15] P. S. Salter, C. Tschierske, S. J. Elston, and E. P. Raynes, *Flexoelectric measurements of a bent-core nematic liquid crystal*, Phys. Rev. E **84**, 031708 (2011).
- [16] T. Porenta, M. Ravnik, and S. Zumer, *Effect of flexoelectricity and order electricity on defect cores in nematic droplets*, Soft Matter **7**, 132 (2011).
- [17] Y. Arakawa, S. Nakajima, R. Ishige, M. Uchimura, S. Kang, G. Konishi, and J. Watanabe, *Synthesis of diphenyl-diacetylene-based nematic liquid crystals and their high birefringence properties*, J. Mater. Chem. **22**, 8394 (2012).
- [18] K. Fodor-Csorba, A. Vajda, G. Galli, A. Jakli, D. Demus, S. Holly, and E. Gacs-Baitz, *Ester-type banana-shaped monomers and investigations of their electro-optical properties*, Macromol. Chem. Phys. **203**, 1556 (2002).
- [19] S. H. Hong, R. Verduzco, J. C. Williams, R. Twieg, E. Di-Masi, R. Pindak, A. Jakli, J. T. Gleeson, and S. Sprunt, *Short-range smectic order in bent-core nematic liquid crystals*, Soft Matter **6**, 4819 (2010); S. Chakraborty, J. T. Gleeson, A. Jakli, and S. Sprunt, *A comparison of short-range molecular order in bent-core and rod-like nematic liquid crystals*, Soft Matter **9**, 1817 (2013).
- [20] C. Bailey, K. Fodor-Csorba, R. Verduzco, J. T. Gleeson, S. Sprunt, and A. Jakli, *Large Flow Birefringence of Nematogenic Bent-Core Liquid Crystals*, Phys. Rev. Lett. **103**, 237803 (2009).
- [21] M. Majumdar, P. Salamon, A. Jakli, J. T. Gleeson, and S. Sprunt, *Elastic constants and orientational viscosities of a bent-core nematic liquid crystal*, Phys. Rev. E **83**, 031701 (2011).
- [22] J. Harden, B. Mbanga, N. Eber, K. Fodor-Csorba, S. Sprunt, J. T. Gleeson, and A. Jakli, *Giant Flexoelectricity of Bent-Core Nematic Liquid Crystals*, Phys. Rev. Lett. **97**, 157802 (2006).
- [23] This field is ~ 120 times higher than the threshold (Frederickz) field needed to orient the director parallel to the surfaces in a 1 mm cell, assuming the “worst” case scenario of strong perpendicular anchoring of the molecular long axis at the surfaces.
- [24] Our previous experiments on the BCN [7], in which only the integrated intensity over solid angle was measured (without the telescope), indicate that the true FWHM of the peaks is $\sim 5^\circ$.
- [25] J. Li, C. H. Wen, S. Gauza, R. Lu, and S. T. Wu, *Refractive Indices of Liquid Crystals for Display Applications*, J. Disp. Technol. **1**, 51 (2005).
- [26] W. Helfrich, *Alignment-Inversion Walls in Nematic Liquid Crystals in the Presence of a Magnetic Field*, Phys. Rev. Lett. **21**, 1518 (1968).
- [27] M. J. E. O'Rourke, D. K. Ding, and E. L. Thomas, *Morphologies and Energies of Neel Inversion Wall Defects in a Liquid Crystal Polyether*, Macromolecules **34**, 6658 (2001).
- [28] S. D. Hudson and E. L. Thomas, *Disclination interaction in an applied field: Stabilization of the Lehmann cluster*, Phys. Rev. A **44**, 8128 (1991).
- [29] A. Sengupta, U. Tkalec, and C. Bahr, *Nematic textures in microfluidic environment*, Soft Matter **7**, 6542 (2011).
- [30] D.-K. Ding, B. Jin, J. Gunther, and E. L. Thomas, *Director textures of the Neel inversion wall in a liquid crystal*

- polymer, Philosophical Magazine B **76**, 951 (1997).
- [31] R. Williams, *Optical rotatory effect in the nematic liquid phase of p-azoxyanisole*, Phys. Rev. Lett. **21**, 342 (1968).
- [32] M. Kleman and C. Williams, *Anchoring energies and the nucleation of surface disclination lines in nematics*, Phil. Mag. **28**, 725 (1973).
- [33] G. Ryschenkow and M. Kleman, *Surface defects and structural transitions in very low anchoring energy nematic thin films*, J. Chem. Phys. **64**, 404 (1976).
- [34] J. Zhou, J. O. Park, G. De Luca, A. D. Rey, and M. Srinivasarao, *Microscopic observations and simulations of Bloch walls in nematic thin films*, Phys. Rev. Lett. **97**, 157801 (2006).
- [35] K. Shia, T. Kosa, P. Palffy-Muhoray, and Y. S. Kim, *Permittivity Gradient Induced Second Harmonic Generation in Periodic Nematic Structure*, Mol. Cryst. Liq. Cryst. **299**, 73 (1997).
- [36] P. N. Butcher and D. Cotter, *The Elements of Nonlinear Optics* (Cambridge University Press, Cambridge, England, 1991), Chapter 5.
- [37] F. Castles, S. C. Green, D. J. Gardiner, S. M. Morris, and H. J. Coles, *Flexoelectric coefficient measurements in the nematic liquid crystal phase of 5CB*, AIP Advances **2**, 022137 (2012).
- [38] In general, the plane of the inversion loop in Fig. 10a can rotate around the field direction (the magnetic free energy is degenerate for such a rotation). This introduces an additional component of the transverse dipole moment along $\hat{\mathbf{z}}$ that for small scattering angle θ contributes at order θ^2 (i.e., negligibly) to the SH intensity.
- [39] The fact that the optical ovens used to heat our samples in 1 mm cuvettes and 0.1 mm thinner cells are different somewhat in design and construction may also contribute to a difference in the thermal gradients produced in the samples during heating or cooling, and thus to a difference in the density of inversion wall defects generated under the applied field.
- [40] J. Prost and J. Marcerou, *On the microscopic interpretation of flexoelectricity*, J. Physique **38**, 315 (1977).
- [41] J. P. Marcerou and J. Prost, *The Different Aspects of Flexoelectricity in Nematics*, Mol. Cryst. Liq. Cryst. **58**, 259 (1980).
- [42] W. Helfrich, *A simple method to observe the piezoelectricity of liquid crystals*, Phys. Lett. **35A**, 393 (1971); *The Strength of Piezoelectricity in Liquid Crystals*, Z. Naturforsch. **26a**, 833 (1971).
- [43] P. J. Ackerman, Z. Qi, Y. Lin, C. W. Twombly, M. J. Laviada, Y. Lansac, and I. I. Smalyukh, *Laser-directed hierarchical assembly of liquid crystal defects and control of optical phase singularities*, Scientific Reports **2**, 414 (2012).
- [44] B. S. Murray, R. A. Pelcovits, and C. Rosenblatt, *Creating arbitrary arrays of two-dimensional topological defects*, Phys. Rev. E **90**, 052501 (2014).
- [45] Q. Wei (private communication).
- [46] See, for example, K. Y. Wong and A. F. Garito, *Third-harmonic-generation study of orientational order in nematic liquid crystals*, Phys. Rev. A **34**, 5051 (1986).
- [47] The sensitivity to single nematic defects (specifically inversion loops of the size shown in Fig. 9) can be improved by reducing the sources of noise associated with background signals, as well as reducing non-sample related background sources such as stray room light. The two main sources of background noise are SH scattering from director fluctuations in the nematic medium and the dark noise of the detection system (camera). For the latter, one can probably do better than our current system with the latest CCD technology optimized for the lowest achievable dark current. Regarding noise arising from director fluctuations, we can offer the following analysis. The average SH power scattered from pinned (or otherwise stabilized) nematic defects is $\bar{P}_{def}^{(2)} \propto N_{def} \left(\frac{E_p}{\tau A}\right)^2 f \tau$, where E_p is the energy per laser pulse incident onto cross-sectional area A of the sample, τ is the temporal pulse width, f is the repetition rate of the pulses, and N_{def} is the number of defects illuminated; for a single defect, $N_{def} = 1$. The average SH power scattered by director fluctuations is $\bar{P}_{def}^{(2)} \propto \frac{V_{illum}}{\langle \xi^3 \rangle} \left(\frac{E_p}{\tau A}\right)^2 f \tau$, with V_{illum} being the illuminated volume of sample and $\langle \xi^3 \rangle$ the average correlation volume for the fluctuations. For single defect detection, the signal-to-noise ratio is therefore $\frac{\bar{P}_{def}^{(2)} T}{\sqrt{\bar{P}_{def}^{(2)} T}} \propto \frac{E_p}{\tau A} \sqrt{\frac{f \tau}{V_{illum}}} \sqrt{T}$ where T is the signal acquisition time. Thus, by focusing from the present $\simeq 1$ mm beam diameter down to $\simeq 10 \mu\text{m}$ and illuminating a single defect while keeping $\frac{E_p}{\tau A}$ constant to avoid damage to the sample, we can obtain a factor of 10 improvement in sensitivity. Another factor of 10 improvement can be realized with a higher duty cycle pulsed laser; a suitable commercial system is available with 100 times larger $f \tau$ than our present laser. Finally, an additional factor of ~ 3 is feasible with 10 times longer integration time T . With these enhancements, and assuming dark noise does not become the limiting factor (we think it would not), SHLS sensitivity to single loops is probably achievable.